Functionalized MoS_2 nanosheet-capped periodic mesoporous organosilicas as a multifunctional platform for synergistic targeted chemo-photothermal therapy

Jianrong Wu,
David H. Bremner,
Shiwei Niu,
Huanling Wu,
Junzi Wu,
Haijun Wang,
Heyu Li,
Li-Min Zhu

PII: S1385-8947(18)30248-1
DOI: https://doi.org/10.1016/j.cej.2018.02.052
Reference: CEJ 18531

To appear in: *Chemical Engineering Journal*

Received Date: 23 November 2017
Revised Date: 2 February 2018
Accepted Date: 10 February 2018

Please cite this article as: J. Wu, D.H. Bremner, S. Niu, H. Wu, J. Wu, H. Wang, H. Li, L-M. Zhu, Functionalized MoS_2 nanosheet-capped periodic mesoporous organosilicas as a multifunctional platform for synergistic targeted chemo-photothermal therapy, *Chemical Engineering Journal* (2018), doi: https://doi.org/10.1016/j.cej.2018.02.052

Functionalized MoS_2 nanosheet-capped periodic mesoporous organosilicas as a multifunctional platform for synergistic targeted chemo-photothermal therapy

Jianrong Wu,[1] David H Bremner[2], Shiwei Niu,[1] Huanling Wu,[1] Junzi Wu,[1] Haijun Wang,[1] Heyu Li,[1] Li-Min Zhu[1,*]

[1]*College of Chemistry, Chemical Engineering and Biotechnology, Donghua University, Shanghai, 201620, PR China*

[2]*School of Science, Engineering and Technology, Kydd Building, Abertay University, Dundee DD1 1HG, Scotland, UK*

[*]Corresponding authors. Email: lzhu@dhu.edu.cn

Abstract: The combination of different therapies into a single platform has attracted increasing attention as a potential synergistic tumor treatment. Herein, the fabrication of a novel folate targeted system for chemo-photothermal therapy by using thioether-bridged periodic mesoporous organosilica nanoparticles (PMOs) as a drug-loading vehicle is described. The novel targeted molecular bovine serum albumin-folic acid-modified MoS_2 sheets（MoS_2-PEI-BSA-FA）were successfully synthesized and characterized, and then utilized as a capping agent to block PMOs to control the drug release and to investigate their potential in near-infrared photothermal therapy. The resulting PMOs–DOX@MoS_2–PEI-BSA-FA complexes–had a uniform diameter (196 nm); high DOX loading capacity (185 mg/g PMOs-SH); excellent photothermal transformation ability; and good biocompatibility in physiological conditions. The PMOs–DOX@MoS_2–PEI-BSA-FA exhibited pH-dependence and near infrared (NIR) laser irradiation-triggered DOX release. *In vitro* experimental results confirmed that the material exhibits excellent photothermal transfer ability, outstanding tumor killing efficiency and specificity to target tumor cells via an FA-receptor-mediated endocytosis process. The *in vivo* experiments further demonstrated that the platform for synergistic chemo-photothermal therapy could significantly inhibit tumor growth, which is superior to any monotherapy. Meanwhile, cytotoxicity assays and histological assessments show that the engineered PMOs@MoS_2–PEI-BSA-FA have good biocompatibility, further inspiring potential biomedical applications. Overall, this work describes an excellent drug delivery system for chemo-photothermal synergistic targeted therapy having good drug release

properties, which have great potential in cancer therapy.

Keywords: Synergistic therapy, periodic mesoporous organosilica, MoS_2, cancer cell targeting, drug delivery

1. Introduction

Nanomaterial-based drug delivery systems are increasingly promising and useful as tools in cancer therapy. Mesoporous silica nanoparticles (MSNs) have been used as carrier systems for drug delivery due to their nontoxic nature, high surface area, large pore volume, tunable pore size and chemically modifiable surfaces [1-3]. Since their discovery in 1999, periodic mesoporous organosilica (PMOs), as a new type of MSNs with an organic group-incorporated, are considered one of the most important developments in this area of research [4,5]. Similar to MSNs, PMOs prepared from organo-bridged alkoxysilanes have tunable mesopores [6]. However, unlike the surface-functionalized MSNs, the porous frameworks of PMOs are based on organic functional groups covalently linking siloxane domains [7-10]. Consequently, the organic moieties in the PMOs are built directly into the walls of the channels that could be utilized for many applications such as gas and molecule adsorption, catalysis, drug and gene delivery, electronics and sensing [11-14]. Guo *et al.* reported that Rhodamine B loaded ethylene-bridged HPMOS NPs functionalized with pH-responsive supramolecular nanovalves enabled the controlled release of the Rhoadamine B at pH 4 or 10 in water and/or in acetonitrile [15]. The first *in vitro* studies on the delivery of drugs were published in 2013 [12] and Lin *et al.* reported a controlled drug release system based on PMOs [16]. Numerous PMO-based controlled release systems have been reported that perfect control over the drugs, achieved largely in the presence of bridged silane with contrary functionality with drug molecules at the pore channels or wall structure [17-21]. Also, preliminary

studies have reported that the PMOs are biodegradable and have better hemo-compatibility than pure mesoporous silica nanoparticles [22,23].

Despite these burgeoning developments, it is still a challenge to produce more general and practical bio-responsive controlled-release PMOs systems. The major problem is that the drugs encapsulated via a non-covalent force often exhibit undesirable premature release during circulation but grafting suitable capping agents onto the surface of PMOs can prevent such problems. Recent reports on the design of capped MSNs have used inorganic nanoparticles [24], polymers [25], peptides [26], drugs [27] and nucleic acid [28] as caps to block the pore entrances of the MSNs. Although there have been considerable successes in the design of capping agents some drawbacks including low drug loading efficiency and limited targeting properties greatly hinder their applications in cancer therapy.

Synergistic therapies are attracting increasing attention in the field of cancer treatment [29,30] and the combination of photothermal therapy with chemotherapy can further enhance the performance in cancer treatment [31-33]. In particular, two-dimensional (2D) transitional metal dichalcogenide (TMDC) nanosheets, such as MoS_2, WS_2, $MoSe_2$ and WSe_2, have received much attention due to their unique electronic, physical and chemical properties [34]. Among them, MoS_2 is an excellent material for biomedical applications because molybdenum is an essential trace element for several cell enzymes and sulfur is a common biological element [35,36]. There have been a number of previous reports using MoS_2 in the area of biomedicine owing to its good biocompatibility and high photothermal performance as shown by

graphene being used to wrap MSNs, gold nanoparticles and gold nanorods [37-41]. Considering the similarities in the morphology and properties between graphene and MoS_2 the latter, in the form of nanosheets, has been investigated as a capping agent to wrap PMOs for drug delivery. Also, because of the excellent photothermal properties of MoS_2 it can act as a thermal gatekeeping coat on PMOs resulting in the design of a novel nanoplatform with photo-triggered drug release and producing synergistic chemo-photothermal therapy. A recent study by Liu et al. reported transferrin-decorated and MoS_2-capped hollow mesoporous silica nanospheres, which show high loading and outstanding chemo–photothermal synergetic efficacy for cancer therapy [42]. However, to the best of our knowledge, there is no report on the validation of both *in vitro* and *in vivo* therapeutic effects of these nanoplatforms.

Generally, designing a multifunctional platform with photothermal ability and targeting properties would be an efficient way to improve the accumulation of chemotherapy drugs, to reduce side effects and synergistically enhance the therapeutic effects. With this in mind, a multifunctional platform based on a functionalized-MoS_2 nanosheet wrapped PMOs was designed for both targeting drug delivery and synergistic chemo-photothermal therapy and is now reported in the present work (Scheme 1). PMO nanoparticles，which have a low density, a uniform diameter (196 nm), a BET surface area of 1023.04 m^2/g, a pore volume of 1.06 cm^3/g, and a uniform pore diameter (D) of 3.84 nm and excellent biocompatibility were first prepared. The chemotherapy drug, DOX, was then loaded into the channels of the PMOs (185 mg DOX per gram of PMOs-SH) and, for the first time, single-layer MoS_2 nanosheets

were prepared followed by modification with folic acid. The MoS_2-LA-BSA-FA complex then acted as capping agent to block PMOs via electrostatic interactions and weak thiol reactions. The drug-release behavior showed that the encapsulated DOX in the PMOs–DOX@MoS_2–LA-PEI-BSA-FA could be controllably released using 808 nm laser irradiation and because of the specific recognition of the FA receptor and MCF-7 expressed on tumor cells, the complexes exhibited excellent targeting ability. Both *in vitro* and *in vivo* experiments demonstrated that the PMOs–DOX@MoS_2–LA-PEI -BSA-FA nanocomposite has an excellent cancer cell killing effect by combined photothermal and chemotherapy, suggesting that the PMOs-based synergistic strategy has great potential in cancer therapy.

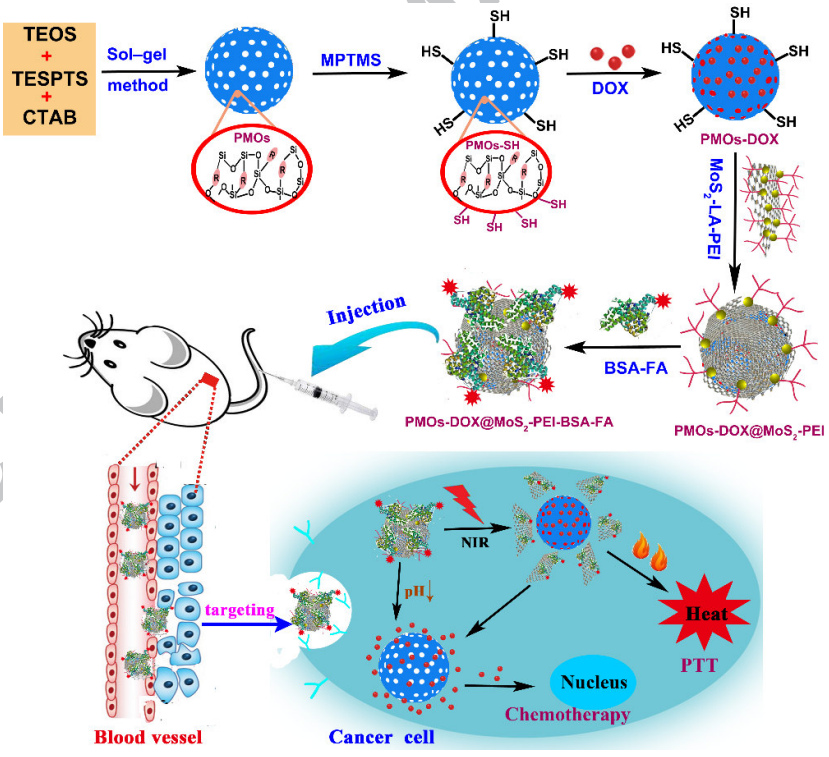

Scheme 1. Schematic illustration for the synthesis and preparation of PMOs–DOX@MoS_2–LA-PEI-BSA-FA composite as a multifunctional drug delivery

system for synergistic chemo-photothermal targeted therapy of tumors.

2. Materials and methods

2.1. Materials

Cetyltrimethyl ammonium bromide (CTAB), tetraethoxysilane (TEOS), concentrated ammonia (25 wt %) and anhydrous ethanol were purchased from Sinopharm Chemical Reagent Co., Ltd (Shanghai, China). Bulk MoS_2 powder (2-8 μm, 99%), 3-mercaptopropyltrimethoxysilane (MPTMS), DOX hydrochloride and 1,4-bis- (triethoxysilyl) propane tetrasulfide (TESPTS) were obtained from Sigma-Aldrich (St. Louis, MO, USA). n-BuLi hexane solution (2.4 M), alpha-lipoic acid (LA), folic acid (FA), N-hydroxysuccinimide (NHS), N-[3-(dimethylamino)propyl]-N′-ethyl-carbodiimide hydrochloride (EDC), 2-(N-morpholino)ethanesulfonic acid（MES）, polyethylenimine (PEI, Mw = 25 kDa) and bovine serum albumin (BSA) were purchased from Aladdin Reagent (Shanghai, China). Dimethyl sulfoxide (DMSO), fetal bovine serum (FBS), phosphate buffered saline (PBS), antibiotics (penicillin/streptomycin) and DMEM media were supplied by the Shanghai Pumai Biotechnology Co. Ltd. 3-(4,5-Dimethylthiazol-2-yl)-2,5-diphenyltetrazolium bromide (MTT) and 4′-6-diamidino-2-phenylindole (DAPI) was purchased from Nanjing Keygen Biotech. The human cancer MCF-7 cell lines and human hepatoma 7402 cells were provided by the Institute of Biochemistry and Cell Biology, Chinese Academy of Sciences. Deionized water (H_2O) used in all experiments was purified by a Millipore system

(Milli-Q, 18.2 MΩ cm).

2.2. Synthesis of PMOs-SH

The thioether-bridged PMOs were prepared according to the surfactant directed sol–gel method. CTAB (0.12 g) was dissolved in a mixture of concentrated aqueous ammonia solution (1 mL, 25 wt %), ethanol (30 mL) and water (75 mL). The solution was heated to 35 ^{o}C for 1 h, and then TESPTS (0.1 mL) and TEOS (0.22 mL) was quickly added under vigorous stirring. The above mixture was stirred for 24 h at 35 ^{o}C, the white product was collected by centrifugation at 10000 rpm for 10 min, washed three times with ethanol and suspended in ethanol (250 mL) and concentrated HCl (0.6 mL) at 60 °C for 3 h to remove the CTAB surfactants.

For the synthesis of PMOs-SH, the prepared PMOs (50 mg) was dispersed in ethanol (150 mL). Then, 3-mercaptopropyltrimethoxysilane (MPTMS; 0.15 mL) and 25 wt % aqueous ammonia solution (0.2 mL) were added and stirred overnight and the PMOs-SH was collected by centrifugation and washed three times with deionized water.

2.3. Synthesis of MoS_2 nanosheets

Multilayered MoS_2 was exfoliated by the Morrison method [43] whereby MoS_2 flake (2 g) was stirred with hexane solution (2 mL) of n-buthyllithium (1.6 M) for 48 h in an N_2 atmosphere. Following the intercalation by lithium, the mixture was washed with hexane to remove residual n-buthyllithium and water (30 mL) was added. The MoS_2-containing water solution was ultrasonicated for 90 min to allow effective exfoliation and then centrifuged at 3000 rpm to remove the multilayered MoS_2

nanosheets and excess LiOH in the precipitates. The exfoliated MoS_2 was dialyzed using a cellulose membrane (MWCO: 10 kDa) for 3 d, then stored as a solution in water. Table S1 gives a summary of the different reaction conditions investigated and the best yield (51.6%) was obtained with 1.6M n-buthyllithium and 90 min sonication.

2.4. Synthesis of MoS_2-PEI–BSA–FA composites.

The outline process for the preparation of MoS_2-PEI–BSA–FA composites is shown in Scheme S1a-b. EDC (260 mg) and NHS (158.8 mg) were added to α–lipoic acid (114.4 mg) dissolved in acetonitrile（25 mL）under vigorous stirring. After 30 min, a solution of PEI (0.5 g) dissolved water (40 mL) with the pH adjusted to 7.4 with dilute hydrochloric acid was added and the solution stirred overnight at room temperature. The resulting product was dialyzed using a cellulose membrane (MWCO: 1 kDa) in pure water for 24 h and then lyophilized to obtain the LA-PEI. The resulting LA–PEI (30 mg) was added into a MoS_2 dispersion in water (10 mL; 0.3 $mg.mL^{-1}$) with 30 min sonication and vigorous stirring to form MoS_2-LA-PEI. In order to remove minor impurities, the product was dialyzed (MWCO: 3500 Da, 4000 rpm, 10 min) with 0.5 M NaCl containing phosphate buffer (20×10^{-3} M) three times and washed with pure water. The final product was stored at 4 °C in water.

The BSA–FA complexes were fabricated following a literature approach as depicted in Scheme S1c [44]. Typically, folic acid (1 mL; 5 mM) in MES buffer solution (5mL; 50 mM; pH 6) was reacted in the dark with EDC (3 mg) and NHS (3 mg) for 20 min. Then the activated FA solution (500 μL; 5 mM) solution was mixed

with BSA (100 mL; 5 μM) and left to stir overnight. Finally, the product was dialyzed for 24 h against MES buffer with a cellulose membrane (MWCO 3500 Da) to remove unreacted FA and reaction by-products. The resulting BSA–FA solution (40 mL) was then mixed with the aqueous solution of MoS_2-LA-PEI followed by the addition of EDC (48 mg) and NHS (28 mg) with stirring for 12 h. This mixed solution was then centrifuged for 15 min at 5000 rpm and washed with water (3 times). Finally, the MoS_2-PEI–BSA–FA nanocomposites were re-suspended in PBS (pH 7.4) solution for further use.

2.5. Preparation of PMOs–DOX@MoS_2-PEI–BSA–FA

PMOs-SH (20 mg) was sonicated for 20 min in PBS solution (10 mL) followed by the addition of DOX dissolved in PBS solution (10 mL: 1 mg/mL) and the suspension was stirred in the dark for 24 h at room temperature. The mixture was centrifuged and washed with PBS (40 mL) and water several times. All supernatants and washed solutions were collected in order to determine the amount of drug loaded using UV-Vis spectrophotometry (482 nm). Finally, the resulting solid material was re-suspended in water (10 mL) and sonicated with a MoS_2-PEI–BSA–FA solution (5 mL: 1.45 mg/mL) for 4 min. The mixture was centrifuged at 11000 rpm for 15 min and then washed with water (three times) to remove any free MoS_2-PEI–BSA–FA and the targeted MoS_2-wrapped PMOs–DOX (PMOs–DOX@MoS_2-PEI–BSA–FA) was obtained after drying at 60 ^{o}C under vacuum. The loading content (LC, w/w%) of DOX were calculated by use of the following equation:

LC= (weight of loaded DOX) / (total weight of nanocomposites) ×100% Eqn 1

2.6. Characterization

Transmission electron microscopy (TEM) was performed on a JEOL JEM-2010 instrument with an acceleration voltage of 200 kV. The surface topology of the obtained materials was analyzed using field emission scanning electron microscopy (SEM, S-4800, Japan, Hitachi). The thickness and size of the MoS_2 were measured with an Agilent 5500 atomic force microscope (AFM, USA) under ambient conditions. Dynamic light scattering (DLS) and zeta potential measurements were performed on a Malvern Zetasizer Nano ZS instrument (ZS90, UK). UV-vis absorption spectra were recorded on a UV-1800 spectrophotometer (Shanghai JingHua Instruments). XRD measurements were performed on a Bruker D8 Advance X-ray diffractometer equipped with graphite-monochromatized Cu Kα radiation (λ=1.5418 Å). Fourier transform infrared (FT-IR) spectra were recorded on a Nicolet Nexus 870 spectrometer (Nicolet Instruments Inc. Madison, WI, USA). Nitrogen sorption isotherms were measured by a Micromeritics Tristar 3000 analyzer (Micromeritics Instruments Corporation, Atlanta, GA, USA). The Mo concentration was determined with a Leeman Prodigy inductively coupled plasma-atomic emission spectroscopy (ICP-AES) system (Hudson, NH03051, USA). The photothermal conversion efficiency of the materials were analyzed using a laser device (Shanghai Xilong Optoelectronics Technology Co. Ltd., Shanghai, China) at a wavelength of 808 nm and the temperature of the solution was monitored using a DT-8891E thermocouple linked to a digital thermometer (Shenzhen Everbest Machinery Industry, Shenzhen, China).

2.7. Photothermal effect of PMOs–DOX@MoS_2-PEI–BSA–FA

In order to measure the photothermal effects, various concentrations of the nanocomposites in PBS (pH 7.4) were irradiated using an 808 nm laser (1 W/cm^2). The influence of laser power density on the photothermal effect was ascertained by irradiating a solution of the PMOs–DOX@MoS_2-PEI–BSA–FA (1 mg/mL) under different power densities; the changes in temperature were measured using PMOs-DOX and PBS as control groups under the same conditions. The thermal stability of PMOs–DOX@MoS_2-PEI–BSA–FA samples was determined by irradiating for 5 min each time with five on-off cycles. Meanwhile, the temperature changes of the different materials under continuous NIR laser irradiation (1 W/cm^2) for 5 min were recorded by using an infrared (IR) thermal imaging system. The photothermal conversion efficiency of PMOs–DOX@MoS_2-PEI–BSA–FA was calculated by the following equation [45]:

$$\eta = \frac{hS(T_{max} - T_{am}) - Q_0}{I(1 - 10^{-A})} \qquad \text{Eqn 2}$$

Where, h is the heat transfer coefficient, S is the surface area, T_{max} is equilibrium temperature, T_{am} is surrounding ambient temperature, Q_0 is heat absorption of the quartz cell, I is the laser power and A is the absorbance of the materials at 808 nm.

2.8. *In vitro* drug release

A dispersion of PMOs–DOX@MoS_2-PEI–BSA–FA in PBS (pH 7.4 or pH 5.0) with a PMOs concentration of 1 mg mL^{-1} was introduced into a dialysis bag (Mw = 8-10 KDa) and then dialyzed against different PBS solutions (40 mL) with exposure

to 808 nm laser irradiation (1 W/cm^2) with shaking (150 rpm) for 10 min. A sample of media released (1 mL) was collected at different time intervals, and an equal volume of fresh buffer was added. The concentration of DOX released was determined by using UV−vis spectrophotometry (484 nm). The control group was treated under identical conditions but without irradiation. The cumulative amount of released DOX from the composites was calculated.

2.9. Cell culture and cytotoxicity assay

MCF-7 cells were cultured in DMEM medium with 10% FBS, 1% penicillin, and 1% streptomycin in a 5% CO_2 incubator at 37 ^oC. The cytotoxicity was quantified by a MTT assay using MCF-7 cells which were seeded in a 96-well plate at 5×10^3 cells per well with 100 μL of DMEM medium. The plate was loaded into an incubator at 37 ^oC under a 5% CO_2 atmosphere for 24 h. The culture medium was removed and replaced with fresh medium (150 μL) containing different concentrations of PMOs-SH or free DOX and the cells were incubated in fresh medium for another 24 h and the MTT solution (100 μL: 5 mg/mL in culture medium) was added. Following incubation for 4 h, the MTT/medium was replaced by DMSO (150 μL) for 20 min to dissolve the formazan crystals. Finally, the absorbance of the solution was determined at 570 nm using a microplate reader (BioTek). Each experiment included six wells for each different condition.

2.10. *In vitro* cellular uptake

Cell targeted efficiency was investigated by utilizing confocal laser scanning microscopy (CLSM) observation and flow cytometry analysis. MCF-7 cells (Folic

acid (FA) receptor positive) and hepatoma 7402 cells (FA receptor negative) were seeded at a density of 1×10^5 cells per well in 24-well plates and cultured for 24 h. All cells were treated with PMOs–DOX@MoS_2-PEI and PMOs–DOX@MoS_2-PEI–BSA–FA at a DOX concentration of 5 μg mL^{-1} for 4 h followed by washing the cells with PBS. The NIR treated group was irradiated with a laser（808 nm）for 5 min at 1.0 W cm^{-2}. The cells in all the groups were cultured for another 2 h and then washed and fixed with 4% formaldehyde for 30 min. The cell nuclei were stained with DAPI and observed by confocal laser scanning microscopy (CLSM, Jena, Germany) equipped with a 63× oil immersion lens.

To correlate the cellular uptake behavior and cell apoptosis by the NPs, MCF-7 cells at a concentration of 1×10^5 cells were allowed attachment growth for 24 h. They were then treated with PMOs–DOX@MoS_2-PEI and the composite NPs with PMOs–DOX@MoS_2-PEI–BSA–FA (DOX concentration of 5 μg/mL) for 12 h with or without 5 min laser irradiation after 2 h incubation. The number of cells that showed early apoptosis (positive for FITC-labeled Annexin V), late apoptosis (double positive for FITC-labeled Annexin V and propidium iodide), and necrosis (positive for propidium iodide) were analyzed by flow cytometry (Becton Dickinson, CA, USA) [15] with untreated cells utilized as blank controls.

Specific cellular uptake of the PMOs–DOX@MoS_2-PEI–BSA–FA within MCF-7 cells and hepatoma 7402 cells was also demonstrated by quantitative ICP-AES analysis. Both MCF-7 and hepatoma 7402 cells were seeded in a 24-well plate at a density of 5×10^5 cells/well and incubated for 24 h. The medium was replaced with

fresh medium containing PMOs–DOX@MoS_2-PEI–BSA–FA and the cells were then incubated for 12 h at 37 ^oC and 5% CO_2. The cells were washed 3 times with PBS, trypsinized, centrifuged, and re-suspended in PBS. The cell suspensions (100 μL) were counted and the remaining cells were centrifuged to form pellets and lysed using an aqua regia solution (0.5 mL) to digest both the cells and the nanoparticles. The digested sample was then diluted with PBS (1.5 mL) and the intracellular concentration of Mo in MCF-7 and hepatoma 7402 cells was quantitatively measured using ICP-AES.

2.11. Synergistic effects of photothermal therapy and chemotherapy *in vitro*

MCF-7 cells were cultured in a 96-well plate at 5×10^3 cells per well for 24 h, and the next day, were co-cultured with PMOs–DOX@MoS_2-PEI–BSA–FA (suspended in medium) or PMOs@MoS_2-PEI–BSA–FA. Cells were divided into six groups: group 1 PBS（control）; group 2 PMOs @MoS_2-PEI-BSA-FA; group 3 free DOX; group 4 PMOs@MoS_2-PEI-BSA-FA+NIR (photothermal therapy); group 5 PMOs-DOX@MoS_2-PEI-BSA-FA nanoparticles (chemotherapy); and group 6 PMOs-DOX@MoS_2-PEI-BSA-FA+NIR (synergistic therapy). After incubation for 12 h, the cells were washed with PBS and culture medium was then added to the wells. The cells were irradiated with a laser (808 nm, 1.0 W cm^{-2}) for 5 min for photothermal and synergistic treatments, and then all the cells were cultured for 24 h and an MTT assay was used to measure cell viability.

2.12. *In vivo* experiments

All the animal experiments were performed in agreement with the guidelines of the Institutional Animal Care and Use Committee. Female athymic nude mice aged 4 to 6 weeks were purchased from Nanjing PengSheng Biological Technology Co., Ltd and subcutaneously injected with 1×10^6 MCF-7 cells per mouse. When the tumors reached 50 mm^3 after cell inoculation, the animals were divided randomly into 6 groups (n = 6 for each group). Each mouse was intravenously injected, via the tail vein, with either: saline (control), PMOs-DOX@MoS_2-PEI–BSA–FA (chemotherapy), free DOX (3 mg/kg), PMOs@MoS_2-PEI–BSA–FA+NIR (photothermal therapy), PMOs–DOX@MoS_2-PEI+NIR, PMOs–DOX@MoS_2-PEI–BSA–FA+NIR (synergistic therapy). The tumors of NIR groups were irradiated with the NIR laser (1 W cm^{-2}) for 5 min on the second day (at 24 h post-injection). The body weight and the tumor volume was measured every 2 days after irradiation and reported as $V = W^2\times L/2$, where W and L are the width and length diameters, respectively.

The biodistribution of PMOs-DOX@MoS_2-PEI–BSA–FA in the tumor-bearing mice was investigated by ICP-AES. A PMOs-DOX@MoS_2-PEI–BSA–FA PBS suspension (0.1 mL; 2 mg/mL) was intravenously injected into the mice. Then the mice were scarified at 12 h post-injection, and the organs were excised, lyophilized, weighted and digested by aqua regia for ICP-AES measurements to determine the Mo content. To compare the difference in the MoS_2 uptake between the PMOs-DOX@MoS_2-PEI–BSA–FA and PMOs-DOX@MoS_2-PEI, the organs and the tumor tissue 12 h post-injection of PMOs-DOX@MoS_2-PEI were extracted and the Mo concentration in those organs was quantified in a similar way.

2.13. Blood biochemistry and pathology

After 20 days of treatment, the representative mice from the six groups were sacrificed to harvest the tumors and the major organs including the heart, liver, spleen, lungs, and kidneys. The tumors and organs were fixed, embedded, sectioned and stained with hematoxylin and eosin (H&E) before optical microscopic observation. Blood samples were collected from the eye vein by removing the eyeball quickly. After 3 h standing at 4 °C, the collected blood samples were centrifuged at 1000 rpm for 3 min to obtain serum. The blood biochemistry analysis was determined using a fully automatic biochemistry analyzer (ADVIA2400, Siemens, USA).

2.14. Statistical analysis

Every experiment was repeated three times and the results are shown as the mean SE ± SD. Graph Pad Prism software was used for the statistical analysis. Student's t-test was used to compare two independent groups of data and $P < 0.05$ was considered significant.

3. Results and discussion

3.1. Synthesis and characterization of nanocomposites

Scheme 1 illustrates the strategy for the construction of the hybrid nanocarriers PMOs–DOX@MoS_2-PEI–BSA–FA. The thioether-bridged PMOs nanospheres were synthesized by a CTAB-directed sol–gel process followed by modification of the thiol bonds in a MPTMS solution. MoS_2 nanosheets were obtained by chemical exfoliation using a previously reported [38] chemical method which was optimized by varying the reaction conditions as shown in Table S1. The highest yield obtained reached

51.6%, which is close to the reported research [46]. The MoS_2 surface was functionalized with LA–PEI (synthesized by a simple amide coupling) which has two sulfur atoms in the LA moiety enabling much stronger binding to the sulfur areas in the MoS_2 and the LA–PEI (Fig. S1a-b, Supporting Information). MoS_2–PEI was then formed by sonication of MoS_2 with LA-PEI，which was then selectively conjugated onto the outer surfaces of PMOs-DOX or PMOs-SH. MoS_2 is remarkably stable and efficiently prevents leakage of the loaded drug. Due to the introduction of amino groups from the PEI, the nanoparticles are functionalized with BSA–FA complexes (Fig. S1c, Supporting Information) through the formation of amide bonds to improve the stealthiness of the nanocarriers under physiological conditions and the capability to target cancer cells [47]. After selective uptake of the nanocarrier via FA receptor mediated endocytosis the nanoparticles are trapped inside the endosome. Under laser irradiation, the MoS_2 transforms NIR light into heat and the local high temperature leads to the expansion and vibration of the MoS_2 sheets and the PMOs, causing DOX release.

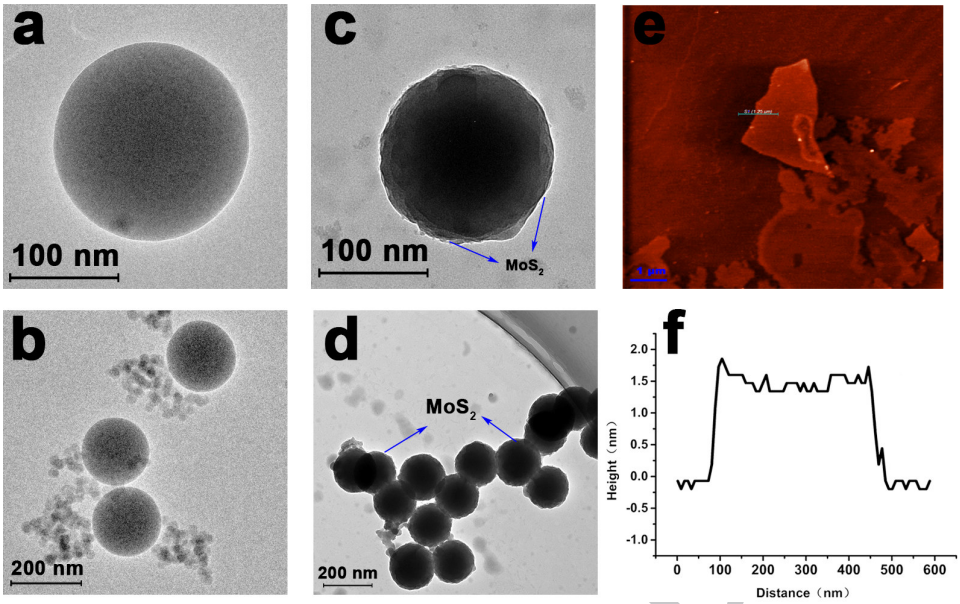

Fig. 1. (a, b) TEM images of thioether-bridged product synthesized by the sol–gel method followed by MPTMS modified PMOs; (c, d) TEM images of PEI modified MoS_2-wrapped DOX-loaded PMOs (PMO–DOX@MoS_2-LA-PEI); the blue arrow in (c,d) indicates the MoS_2 nanosheets on PMOs; (e) AFM topography images of the as-exfoliated MoS_2 nanosheets and (f) the corresponding height profile.

The TEM images (Fig. 1a-b) show that the prepared PMOs have well-defined spherical nanostructures with a diameter of approximately 196 nm. In addition, the SEM images reveal that PMOs have similar spherical morphology with an average diameter around 200 nm (Fig. S1, Supporting Information), which is further verified by the particle size distribution of PMOs measured by TEM. The structures of the PMOs were also studied by X-ray diffraction (XRD) and the XRD pattern shows a strong peak at 2.26°, suggesting the PMOs have an ordered mesostructure (Fig. S2, Supporting Information). The results of the N_2 adsorption–desorption isotherm and pore size distribution curve (Fig. S3, Supporting Information) indicated that the

PMOs-SH possess a large BET surface area (1023.04 m^2/g), a pore volume of 1.06 cm^3/g, and uniform pore diameter (D) of 3.84 nm. The mercaptopropyl groups in the thiol-modified PMOs were identified by Raman spectroscopy with the C-H stretching of the CH_2 groups appearing at 2931 cm^{-1}. The Si-C bond stretching can be identified at 1424 cm^{-1} and the Si-O-Si bond vibration is at 786 cm^{-1}. Other vibrations are observed at 1328 cm^{-1} (symmetric deformation of the CH-S group) and 621 cm^{-1} (C-S bond stretching) indicating the existence of sulfydryl groups in the PMOs-SH. Furthermore, as shown in the FT-IR spectra (Fig. S4, Supporting Information), the PMOs-SH (black line) demonstrate the characteristic C-H bonds at 2831 cm^{-1}; the C-S bond at 682 cm^{-1}; and an -SH bond at 576 cm^{-1}, all of which is consistent with the published literature [17]. After DOX was loaded into the PMOs (red line), the absorption at 1695 cm^{-1}, which can be assigned to C=O stretching of DOX, also verifies that the desired materials were successfully prepared. In addition, the DOX-loading capacity reached 185 mg DOX per gram of PMOs-SH.

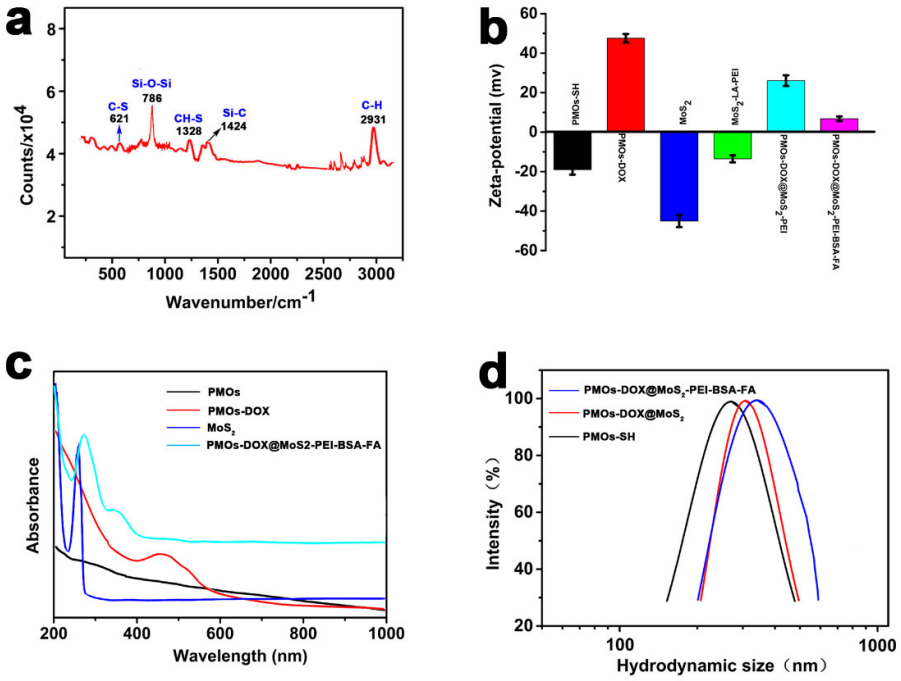

Fig. 2. (a) Raman spectra of thiol-modified PMOs; (b) Zeta potentials of PMOs-SH, PMOs-DOX, MoS_2 nanosheets, MoS_2-LA-PEI, PMOs-DOX@MoS_2-PEI, and PMOs-DOX@MoS_2-PEI-BSA-FA in distilled H_2O; (c) UV-Vis absorption spectra of the PMOs, PMO–DOX, MoS_2, and PMO–DOX@MoS_2-PEI-BSA-FA; and (d) Hydrodynamic diameters of the PMOs-SH, PMO–DOX@MoS_2, and PMO–DOX@MoS_2–PEI-BSA-FA.

After the PMOs-DOX was mixed with the targeted-MoS_2 under sonication in water for a few minutes PMOs–DOX@MoS_2-PEI–BSA–FA was obtained. As revealed by TEM (Fig. S5, Supporting Information) the prepared MoS_2 nanosheets were mostly single-layer sheets with sizes in the range 120–300 nm. AFM imaging revealed that the MoS_2-LA-PEI flakes have a thickness of about 1.5-2 nm, which corresponds to a single layer（Fig. 1e-f). The TEM images (Fig. 1b-c) show that MoS_2 nanosheets were successfully wrapped around the surface of the PMOs–DOX. Zeta

potential analysis was performed to investigate the changes in surface charge of the prepared nanocomposites during the whole process. The zeta potential of PMOs-SH was −19.0 mV, which changed to +47.6 mV when loaded with DOX. The MoS_2 flakes exhibited a zeta potential of -45.0 mV, which changed to -13.5 mV on coating with LA-PEI. The formation of PMOs-DOX@MoS_2-PEI still showed a positive potential of +26.1 mV and, after BSA–FA grafting, the zeta potential of the resulting PMOs–DOX@MoS_2-PEI–BSA–FA dropped to 6.8 mV, further confirming the successful loading of DOX, the wrapping of MoS_2 and modification of the targeted region. The UV-Vis absorption spectrum of the PMOs–DOX@MoS_2-PEI–BSA–FA indicates the presence of MoS_2 nanosheets with the absorption peaks at 255 nm, further demonstrating the successful wrapping of MoS_2 around the PMOs–DOX (Fig. 2c). Furthermore, the absorption peak of DOX (484 nm) in PMOs–DOX, indicates that the drug had been loaded into the PMOs. Meanwhile, the presence of the folate functionality was confirmed by the UV spectrum of PMOs–DOX@MoS_2-PEI–BSA–FA showing the characteristic folic acid absorption peak at 362 nm. Thus, this, along with the absorption peaks of MoS_2 nanosheets shows that the MoS_2-PEI–BSA–FA was successfully prepared. Additionally, PMOs–DOX@MoS_2-PEI–BSA–FA display strong absorbance in the NIR region, while PMOs show virtually none in that region, demonstrating the potential of targeted-MoS_2 as a photothermal therapy on irradiation. The IR spectrum of the folic acid conjugate (Fig. S4a, Supporting Information) shows a strong alkyl C−H stretch at 2850 cm^{-1} and the bonds at 1504 cm^{-1} from the FA molecule. The vibration bands at

1705 and 3450 cm^{-1} indicate successful folic acid binding, which is due to the linkage between the NH_2 group of the folic acid conjugates and the COOH group of the BSA. Furthermore, some characteristic bands of PMOs-DOX had almost disappeared indicating the modified-MoS_2 wrapping. The hydrodynamic diameters of the nanocomposites were verified by dynamic light scattering (DLS). After wrapping with the MoS_2 nanosheets, the hydrodynamic diameter of the resulting PMOS–DOX@MoS_2–PEI–BSA–FA is 314 nm, which is increased compared to PMOs–SH (259 nm). The size difference of the PMOs–DOX@MoS_2–PEI–BSA–FA and PMOs-SH measured by TEM and DLS is mainly attributed to the presence of water [15]. In addition, the PMOs–DOX@MoS_2–PEI–BSA–FA showed higher colloidal stability and were well dispersed in water, PBS and cell culture medium without any agglomeration even after 12 h on standing (Fig. S6, Supporting Information). Meanwhile, the colloidal stability of PMOs–DOX@MoS_2–PEI–BSA–FA was further investigated by measuring the hydrodynamic size. Clearly, the hydrodynamic size of the particles do not show any significant changes after 7 days, suggesting that the developed PMOs–DOX@MoS_2–PEI–BSA–FA nanoparticles possess good colloidal stability.

3.2. Photothermal effect

Owing to the ability of PMOs–DOX@MoS_2–PEI–BSA–FA nanoparticles to convert NIR light energy into heat, the photothermal conversion efficiency was investigated by measuring the dispersion temperature under 808 nm NIR irradiation. As shown in Fig. 3a, a concentration-dependent photothermal heating effect (1 W/cm^2

for 5 min) is observed and Fig. 3b shows the laser-power-dependent photothermal effect with different irradiation power densities of the PMOs–DOX@MoS_2–PEI–BSA–FA (1 mg mL^{-1}). In contrast to the negligible temperature change of pure water, a significant increase to 53.7 °C was observed when PMOs–DOX@MoS_2–PEI–BSA–FA (2.0 mg mL^{-1}) was irradiated for 5 min at 1.0 $W \cdot cm^{-2}$, indicating suitability for photothermal therapy [31]. In comparison, PMOs–DOX solutions without MoS_2 wrapping showed an unexplainable temperature rise at the same irradiation conditions. Also, with the increase of laser power density from 0.5 to 2.0 $W \cdot cm^{-2}$ (Fig. 3b) the temperature of the dispersion is also remarkably enhanced and the dispersion shows excellent photothermal stability, confirming it as a promising candidate for photothermal therapy with five on/off cycles of laser irradiation (Fig. 3c). As shown in Fig. 3d, the solution temperatures of MoS_2 and PMOs-DOX@MoS_2-PEI-BSA-FA both increased rapidly under the 808 nm laser irradiation (1 W/cm^2) and reached 50.7 °C and 45.8 °C respectively, within 5 min at the same MoS_2 concentration. In comparison, the water and PMOs-DOX solution remained below 30 °C under the same laser irradiation. Meanwhile, the photothermal conversion efficiency of PMOs–DOX@MoS_2–PEI–BSA–FA was calculated to be 62.5% and the linear regression curve is shown in Fig. 3e.

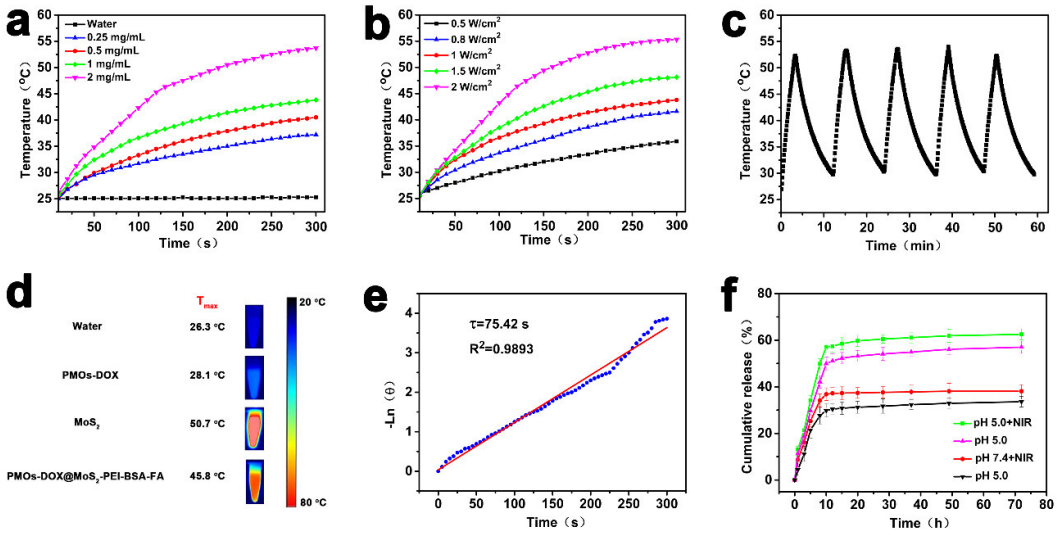

Fig. 3. (a) Temperature variation curves of the PMOs–DOX@MoS_2–PEI-BSA-FA solutions with different concentrations at a laser power density of 1 W cm^{-2} for 5 min. (b) Temperature variation curves of the PMOs–DOX@MoS_2–PEI-BSA-FA solution at different laser power densities for 5 min. (c) Temperature plot of PMOs–DOX@MoS_2–PEI-BSA-FA solution irradiated by an 808 nm laser (2 W cm^{-2}) for five on–off cycles. (d) Photothermal images of water, PMOs-DOX, MoS_2, and PMOs–DOX@MoS_2–PEI-BSA-FA suspensions under continuous NIR laser irradiation (1 W/cm^2) for 5 min. (e) The linear regression curve between the cooling stage and negative natural logarithm of driving force temperature of PMOs–DOX@MoS_2–PEI-BSA-FA. (f) DOX release profiles from PMOs–DOX@MoS_2–PEI-BSA-FA nanocomposites at different pH with or without NIR laser irradiation (808 nm, 1 W/cm^2).

3.3. Drug release *in vitro*

To evaluate the potential of using PMOs–DOX@MoS_2–PEI–BSA–FA as a drug delivery system, the *in vitro* controllable drug release behavior of the nanocarrier with

and without laser irradiation were investigated at different time points and pHs. The released DOX from the PMOs–DOX@MoS_2–PEI–BSA–FA was less than 2% without laser irradiation after 1 h (Fig. S7, Supporting Information). In contrast, DOX release exceeded 15% after 1 h laser irradiation, which was higher than that without irradiation. These results indicate that the NIR light-triggered photothermal heating effect could promote the release of DOX. This behavior may be attributed to the MoS_2 region inducing hyperthermia under laser irradiation, which leads to the vibration of the MoS_2 nanosheets and PMOs-SH and consequently decreases the interaction between DOX and the nanoplatforms. Furthermore, the release profiles of DOX indicated a pH-responsive pattern. As can be seen in Fig. 3f, DOX was released more quickly at pH 5.0 than pH 7.4 and the cumulative release was greatest at pH 5 with irradiation. The phenomenon can be attributed to the reduction of interaction (hydrophobic interaction and electrostatic interaction) of DOX with the PMOs at low pH, which is beneficial for tumor treatment because they are more acidic than normal tissues [39]. Therefore, the pH-dependent and NIR-stimulated release of DOX could effectively enhance the synergistic chemo-photothermal therapeutic effect for tumor treatment.

3.4. Cellular uptake

Targeted delivery is a critical requirement of nanomedicine. Nanocarriers with a targeting ligand can recognize and bind with the receptor expressed on the cell surface, which triggers receptor-mediated endocytosis and increases the level of uptake. MCF-7 cells (FA receptor positive) and hepatoma 7402 cells (FA receptor negative)

were chosen as model cancer cells to study, using confocal laser scanning microscopy, the capacity of FA in the cellular uptake of PMOs–DOX@MoS_2-PEI–BSA–FA (Fig. 4). Both cell lines could uptake PMOs–DOX@MoS_2-PEI–BSA–FA and PMOs–DOX@MoS_2-PEI, as shown by DAPI (blue) and DOX (red) fluorescence. Fig. 4a and b also indicates that the cells incubated with PMOs–DOX@MoS_2-PEI–BSA–FA exhibit much stronger DOX fluorescence than those of PMOs–DOX@MoS_2-PEI, which confirms that the cellular uptake of PMOs–DOX@MoS_2-PEI–BSA–FA is related to the FA receptor-mediated endocytosis of the MCF-7 cells. In comparison, PMOs–DOX@MoS_2 -PEI–BSA–FA and PMOs–DOX@MoS_2-PEI exhibited similar uptake and rather weak DOX fluorescence in the hepatoma 7402 cells, owing to the lack of an FA receptor (Fig. 4b). These results corroborate the view that nanocomposites modified with FA facilitate recognition by MCF-7 cells and enhance the cellular uptake. Flow cytometry was also adopted to investigate the uptake of PMOs–DOX@MoS_2-PEI–BSA–FA by MCF-7 cells and to evaluate the induction of apoptosis by chemo-photothermal treatment. The increased fluorescence of DOX (Fig. S8, Supporting Information) indicated the uptake of PMOs–DOX@MoS_2-PEI–BSA–FA was higher than that of PMOs–DOX@MoS_2-PEI, further evidencing the specific FA-mediated cancer cell targeting. Furthermore, the cell apoptosis by flow cytometry analysis was performed as shown in Fig. 5a. The PMOs–DOX@MoS_2-PEI–BSA–FA treatment greatly increased cell apoptosis compared to just the PMOs–DOX@MoS_2-PEI and the control and, interestingly, the laser irradiation itself had a slight effect on cell viability.

Incubation with PMOs–DOX@MoS_2-PEI and PMOs–DOX@MoS_2-PEI–BSA–FA for 12 h induced apoptosis up to 13.8% and 33.9%, respectively. With laser irradiation, the PMOs–DOX@MoS_2-PEI–BSA–FA was more effective in induction of apoptosis than PMOs–DOX@MoS_2-PEI (59.3% vs 43.1%), further verifying the promoted apoptosis and higher cytotoxicity of the targeted drug delivery system.

The targeting specificity of the PMOs–DOX@MoS_2-PEI–BSA–FA complexes was further proven by quantitative ICP-AES analysis of the Mo uptake in MCF-7 cells and hepatoma 7402 cells (Fig. 5b). The Mo uptake in the MCF-7 cells is 1.75, 1.9 and 1.6 times higher than that in hepatoma 7402 cells at the same concentration. The above results demonstrate that the cellular uptake of the PMOs–DOX@MoS_2-PEI–BSA–FA might be via the FA-receptor-mediated endocytosis process.

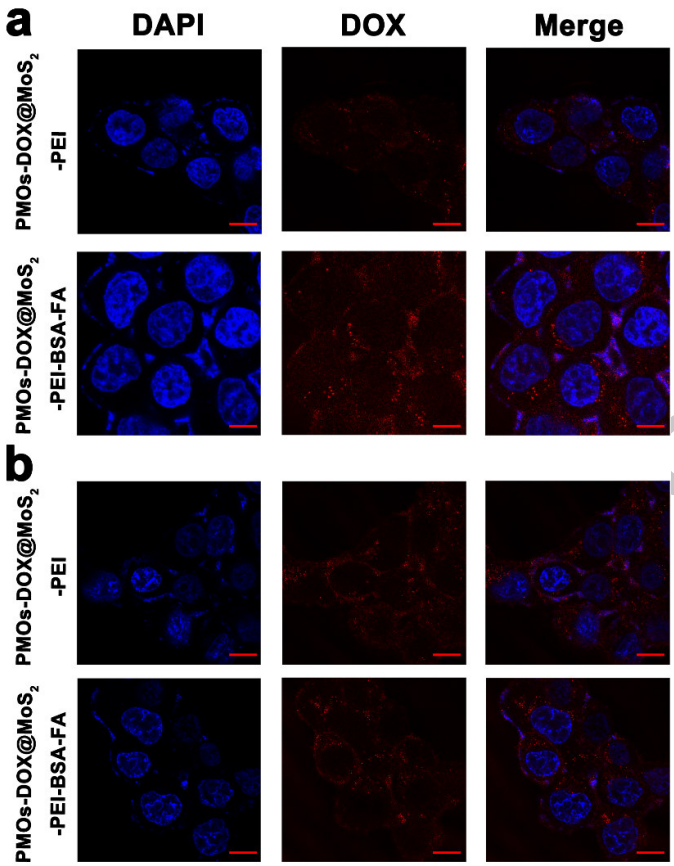

Fig. 4. Confocal laser scanning microscopy of (a) MCF-7 and (b) hepatoma 7402 cells treated with PMOs–DOX@MoS_2-PEI and PMOs–DOX@MoS_2-PEI–BSA–FA for 4 h (relative DOX = 5.0 μg/mL). (Blue fluorescence is associated with DAPI; red fluorescence is expressed by released DOX and DOX in the PMOs.).

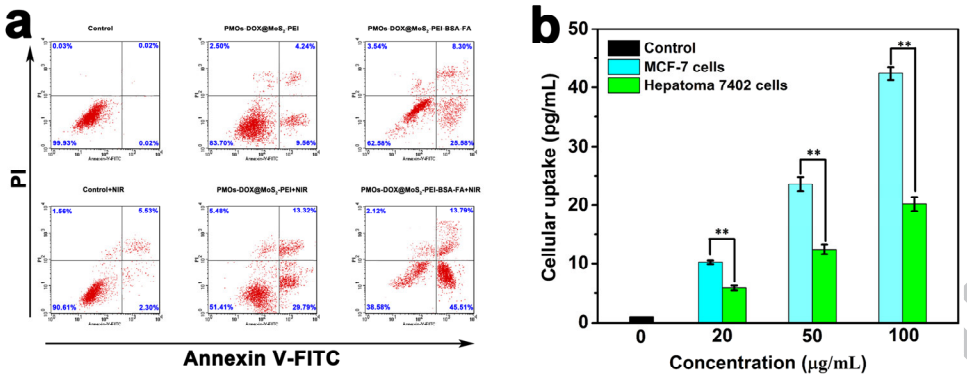

Fig. 5. (a) Flow cytometric analysis of the apoptosis of MCF-7 cells for 12 h induced by PMOs–DOX@MoS_2-PEI and PMOs–DOX@MoS_2-PEI–BSA–FA with or without laser irradiation (Annexin V-FITC/PI staining; DOX concentrations 5 μg/mL). (b) Cellular uptake of Mo in MCF-7 and hepatoma 7402 cells treated with the PMOs–DOX@MoS_2-PEI–BSA–FA at different concentrations for 12 h.

3.5. *In vitro* cytotoxicity assays

A MTT assay was performed to investigate the viability of MCF-7 cells after incubating with the various concentrations of PMOs@MoS_2–PEI–BSA–FA, MoS_2 or PMOs-SH. As shown in Fig. 6a, both the PMOs@MoS_2–PEI–BSA–FA and PMOs-SH nanocomposites showed no obvious cytotoxicity on MCF-7 cells, with cell viability remaining over 80% in the concentration range from 0.1 to 100 μg/mL. In particular, the PMOs@MoS_2–PEI–BSA–FA exhibits excellent cell compatibility even at a high concentration of 100 μg/mL.

3.6. *In vitro* synergistic therapeutic efficacy

To investigate the synergistic therapeutic efficacy of the PMOs–DOX@MoS_2-PEI–BSA–FA against cancer cells, different treatments were carried out by incubation with MCF-7 cells, followed by a MTT assay. Considering

the low cytotoxicity of PMOs@MoS_2-PEI–BSA–FA, the killing effect of PMOs–DOX@MoS_2-PEI–BSA–FA against MCF-7 cells was measured. Fig. 6b shows that cell death in each group of PMOs–DOX@MoS_2-PEI–BSA–FA was dose dependent under the same irradiation conditions. At a DOX level of 1 $\mu g.mL^{-1}$, more than half of the cells were killed in the PMOs–DOX@MoS_2-PEI–BSA–FA and free DOX groups, but in the PMOs–DOX@MoS_2 group more than 70% of the cells survived when the DOX was 2 $\mu g.mL^{-1}$. This may be explained by the special affinity of FA to the FA receptor inducing higher internalization efficiency by MCF-7 cells. The therapeutic efficacy of the PMOs–DOX@MoS_2-PEI–BSA–FA for cancer cells was also investigated and it can be seen that the viability of cells with different treatments significantly decreased after 24 h (Fig. 6c) or 48 h (Fig. 6d), while the cell viability of the control groups (PBS, PMOs@MoS_2-PEI–BSA–FA) showed no obvious decrease. The individual groups (DOX and PMOs–DOX@MoS_2-PEI–BSA–FA) with an equivalent dose of DOX, clearly exhibited marked cytotoxicity (Fig. 6c,d), confirming the chemotherapy effect of PMOs–DOX@MoS_2-PEI–BSA–FA. Meanwhile, the cell viabilities in PTT groups were much lower than control groups, indicating the PTT effect of the nanocomposites. The cell viabilities in the synergistic therapy group were much lower than in the monotherapy groups (chemotherapy or PTT). These significant results demonstrate that the synergistic therapy by PMOs–DOX@MoS_2-PEI–BSA–FA can kill cancer cells. The information obtained from the *in vitro* release and cell viability results (Fig. 3f) demonstrates that (1) the constructed multifunctional platform is an

excellent controlled release system, and (2) NIR laser irradiation not only induces heat for photothermal therapy, but also accelerates the release of DOX from PMOs–DOX@MoS_2-PEI–BSA–FA leading to enhanced chemotherapy.

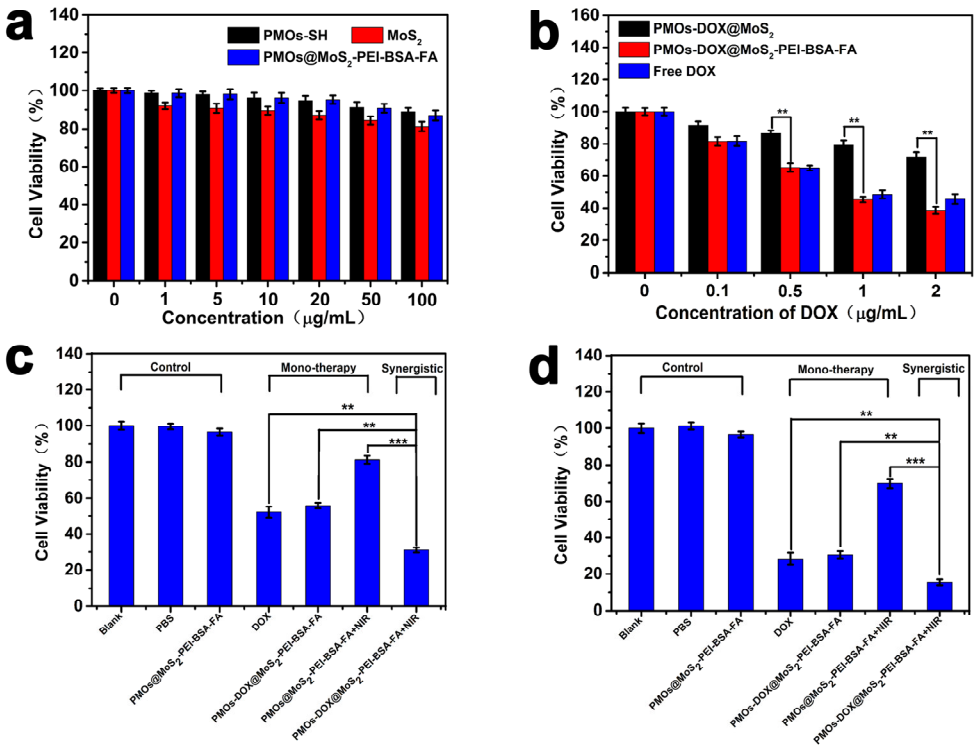

Fig. 6. *In vitro* antitumor activity against MCF-7 cells: (a) Cell viabilities of MCF-7cells incubated with PMOs-SH, MoS_2 and PMOs@MoS_2-PEI–BSA–FA nanoparticles at various concentrations. (b) Cell viability of MCF-7 cells incubated with different concentrations of DOX, PMOs-DOX and PMOs–DOX@MoS_2-PEI–BSA–FA (with equivalent concentrations of DOX). (c) and (d) Cell viability of MCF-7 cells treated with different nanocomposite with or without 808 nm laser irradiation and then incubated for 24 h (c) or 48 h (d). (The total drug content in all groups was kept the same). Independent-samples t test $^{**}P < 0.01$, $^{***}P < 0.001$.

3.7. Antitumor effect *in vivo*

Inspired by the excellent chemo-photothermal synergistic therapy effect *in vitro* of PMOs–DOX@MoS_2-PEI–BSA–FA, the *in vivo* therapeutic effect was investigated by measuring tumor size (Fig. 7). When tumors grew to about 50 mm^3 in volume, mice were treated with PMOs–DOX@MoS_2-PEI–BSA–FA and PMOs-DOX@MoS_2-PEI (3 mg DOX equiv./kg) and irradiated with NIR laser (808 nm, 1 W/cm^2, 5 min) at 8 h post injection. The treatment was repeated once a week with PMOs–DOX@MoS_2-PEI–BSA–FA without NIR, PMOs@MoS_2-PEI-BSA-FA with NIR irradiation; with free DOX and saline being used as controls. The results show that PMOs–DOX@MoS_2-PEI–BSA–FA with NIR irradiation can inhibit tumor growth much better owing to the synergistic chemo-photothermal therapy (Fig. 7a-7b). Meanwhile, the results also showed that mice treated with PMOs–DOX@MoS_2-PEI–BSA–FA and NIR irradiation inhibited tumor growth by interacting with the targeted region (FA), which was obviously more effective than non-targeting PMOS-DOX@MoS_2-PEI under the same conditions. In addition, the chemotherapy group (PMOs–DOX@MoS_2-PEI–BSA–FA or DOX) or photothermal therapy (PMOs@MoS_2-PEI-BSA-FA with laser irradiation) alone can also inhibit tumor growth, but is not as efficacious as that in the synergistic therapy group. Free DOX treatment could also inhibit tumor growth but was not as effective as PMOs–DOX@MoS_2-PEI–BSA–FA with NIR irradiation. The photographs of tumors isolated at day 20 from the mice treated with PMOs–DOX@MoS_2-PEI–BSA–FA demonstrate the good antitumor efficacy *in vivo* (Fig. 7b). In addition, no weight loss

was observed in any of the groups, indicating the high bio-safety of the materials (Fig. 7c). Meanwhile, the Kaplan–Meier survival curve showed that mice treated with PMOs–DOX@MoS_2-PEI–BSA–FA in combination with NIR irradiation had a much longer survival period than for the other groups (Fig. 7D), demonstrating satisfactory biocompatibility and biosafety of the *in vivo* application.

The bio-distribution of Mo in tumor tissue and several major organs (heart, lung, spleen, liver, kidney and tumor) was studied by ICP-AES at 12 h post intravenous injection of both PMOs–DOX@MoS_2-PEI–BSA–FA and PMOs–DOX@MoS_2-PEI (Fig. S9). Notably, the PMOs–DOX@MoS_2-PEI–BSA–FA was mainly retained in the liver and spleen, both of which are major organs of the reticulo-endothelial system (RES).In addition, compared with the PMOs–DOX@MoS_2-PEI, the PMOs–DOX@MoS_2-PEI–BSA–FA appeared to have less tendency to be accumulated in the other major organs, but to be taken up by the tumor site. This further suggests that the special FA-mediated active targeting role.

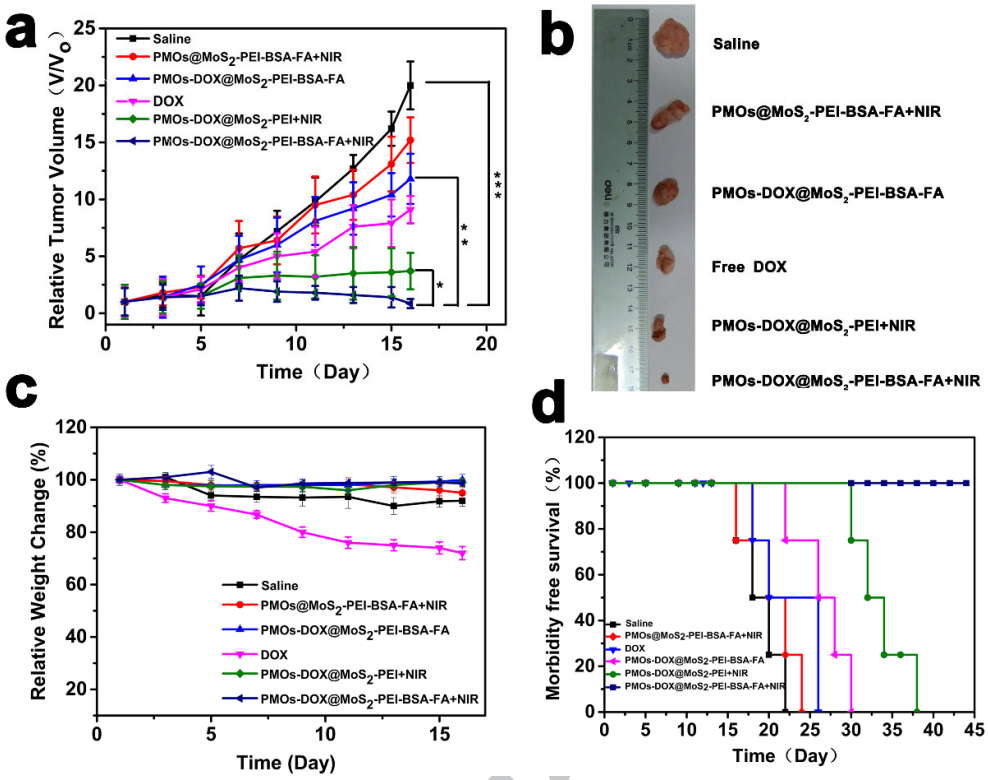

Fig. 7. *In vivo* synergistic chemo-photothermal effect of PMOs–DOX@MoS_2-PEI–BSA–FA with NIR irradiation. (a) Relative tumor growth curves of the MCF-7 tumor-bearing nude mice after intravenous injection of the various treatment samples (n = 6); *p < 0.05, **p < 0.01, and ***p < 0.001 (Student's t test). (b) Typical photographs of MCF-7 tumor-bearing mice on day 20. (c) The average body weights of mice after various treatments. (d) Morbidity-free survival rates of mice in different treatment groups within 43 d.

3.8. HE staining and blood biochemistry

The *in vivo* toxicity of PMOs–DOX@MoS_2-PEI–BSA–FA was evaluated by histological analysis with H&E staining using sections obtained from the major organs of the mice (heart, liver, spleen, lung and kidney) as described in Section 2.12. As shown in Fig. 8, no obvious side effects were found in these tissues, no apparent

inflammation, injury, and no necrosis was observed, confirming the negligible long-term toxicity. Meanwhile, blood biochemical analyses were carried out and various serum biochemical indicators were measured to detect the antitumor efficacy of the PMOs–DOX@MoS_2-PEI–BSA–FA (Fig. S10, Supporting Information). Considering all the biochemical indicators, no statistically significant difference was observed between the control group and the PMOs–DOX@MoS_2-PEI–BSA–FA groups. Hence, the synergistic treatment does not affect the blood chemistry of mice. Furthermore, since ALT, AST and CRE are closely related to the functions of the liver and kidney of mice, the results demonstrated that no liver or kidney toxicity was induced by treatment, suggesting the safe application of PMOs–DOX@MoS_2-PEI–BSA–FA in cancer therapy.

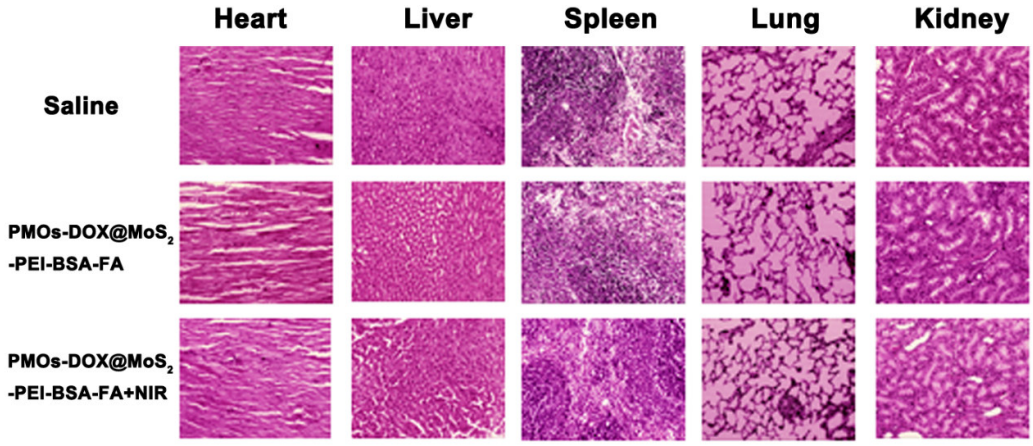

Fig. 8. Representative H&E sections of organ tissues (heart, liver, spleen, lung, and kidney) of tumor-bearing mice after treatment with either saline, PMOs–DOX@MoS_2-PEI–BSA–FA or PMOs–DOX@MoS_2-PEI–BSA–FA + NIR.

4. Conclusions

In summary, novel multifunctional PMOs–DOX@MoS_2-PEI–BSA–FA platforms were successfully synthesized and then studied for synergistic chemo-photothermal therapy. MoS_2 nanosheets were wrapped onto DOX-loaded PMOs-SH and then modified with the targeting moiety BSA-FA. The prepared PMOs–DOX@MoS_2-PEI–BSA–FA had a uniform diameter (196 nm), high drug-loading capacity (185 $mg.g^{-1}$ PMOs-SH), exhibited good biocompatibility and outstanding photothermal properties under NIR laser irradiation. The fabricated multifunctional platform possess the following properties: (1) A high loading efficiency of DOX for chemotherapy. (2) The MoS_2 nanosheets, as the capping agent, block the pores of PMOs to reduce the sudden release of DOX into the blood and effectively absorb and convert NIR light to heat for photothermal therapy. (3) The nanocomposites can be specifically delivered into MCF-7 cells via a receptor-mediated endocytosis pathway utilizing FA targeting. (4) The loaded DOX shows a significant dual stimuli-responsive release by a photo-response in an acidic environment. Notably, the *in vitro* and *in vivo* experimental results showed that the PMOs–DOX@MoS_2-PEI–BSA–FA showed a synergistic chemo-photothermal therapy, which was significantly superior to each individual therapy. Thus, this outstanding multifunctional platform has the potential to be a drug delivery system for multimodal antitumor therapy.

AUTHOR INFORMATION

Corresponding Authors

*E-mail: lzhu@dhu.edu.cn. Phone: +86 021 67792655.

Author Contributions

All authors have given approval to the final version of the manuscript.

Acknowledgements

This research was financially supported by grant 16410723700 from the Science and Technology Commission of Shanghai Municipality, the Biomedical Textile Materials "111 Project" of the Ministry of Education of China (No B07024), and the UK-China Joint Laboratory for Therapeutic Textiles (based at Donghua University).

References

[1] C.L. Zhu, C.H. Lu, X.Y. Song, H.H. Yang, X.R. Wang, Bioresponsive controlled release using mesoporous silica nanoparticles capped with aptamer-based molecular gate, J. Am. Chem. Soc. 133 (2011) 1278-1281.

[2] T. Suteewong, H. Sai, R. Cohen, S. Wang, M. Bradbury, B. Baird, S.M. Gruner, U. Wiesner, Highly aminated mesoporous silica nanoparticles with cubic pore structure, J. Am. Chem. Soc. 133 (2011) 172-175.

[3] Y.-S. Lin, C.L. Haynes, Synthesis and characterization of biocompatible and size-tunable multifunctional porous silica nanoparticles, Chem. Mater. 21 (2009) 3979-3986.

[4] R. Mo, Q. Sun, N. Li, C. Zhang, Intracellular delivery and antitumor effects of pH-sensitive liposomes based on zwitterionic oligopeptide lipids, Biomaterials 34 (2013) 2773-2786.

[5] S.G. Shinji Inagaki, Yoshiaki Fukushima, Tetsu Ohsuna, Osamu Terasaki, Novel mesoporous materials with a uniform distribution of organic groups and inorganic oxide in their frameworks, J. Am. Chem. Soc. 121 (1999) 9611-9614.

[6] J.G. Croissant, X. Cattoen, M.C. Wong, J.O. Durand, N.M. Khashab, Syntheses and applications of periodic mesoporous organosilica nanoparticles, Nanoscale 7 (2015) 20318-20334.

[7] N. Mizoshita, Y. Goto, Y. Maegawa, T. Tani, S. Inagaki, Tetraphenylpyrene-bridged periodic mesostructured organosilica films with efficient visible-light emission, Chem. Mater. 22 (2010) 2548-2554.

[8] M. Ohashi, M. Aoki, K. Yamanaka, K. Nakajima, T. Ohsuna, T. Tani, S. Inagaki, A periodic mesoporous organosilica-based donor-acceptor system for photocatalytic hydrogen evolution, Chem. Eur. J. 15 (2009) 13041-13046.

[9] Y. Yamamoto, H. Takeda, T. Yui, Y. Ueda, K. Koike, S. Inagaki, O. Ishitani, Efficient light harvesting *via* sequential two-step energy accumulation using a Ru–Re5 multinuclear complex incorporated into periodic mesoporous organosilica, Chem. Sci. 5 (2014) 639-648.

[10] X. Meng, T. Yokoi, D. Lu, T. Tatsumi, Synthesis and characterization of chiral periodic mesoporous organosilicas, Angew. Chem. Int. Ed. 46 (2007) 7796-7798.

[11] J. Liu, H.Q. Yang, F. Kleitz, Z.G. Chen, T. Yang, E. Strounina, G.Q.M. Lu, S.Z. Qiao, Yolk-shell hybrid materials with a periodic mesoporous organosilica shell: ideal nanoreactors for selective alcohol oxidation, Adv. Funct. Mater. 22 (2012) 591-599.

[12] Y. Chen, P. Xu, H. Chen, Y. Li, W. Bu, Z. Shu, Y. Li, J. Zhang, L. Zhang, L. Pan, X. Cui, Z. Hua, J. Wang, L. Zhang, J. Shi, Colloidal HPMO nanoparticles: silica-etching chemistry tailoring, topological transformation, and nano-biomedical applications, Adv. Mater. 25 (2013) 3100-3105.

[13] M.A.O. Lourenço, P. Figueira, E. Pereira, J.R.B. Gomes, C.B. Lopes, P. Ferreira, Simple, mono and bifunctional periodic mesoporous organosilicas for removal of priority hazardous substances from water: The case of mercury(II), Chem. Eng. J. 322 (2017) 263-274.

[14] G. Morales, R. van Grieken, A. Martín, F. Martínez, Sulfonated

polystyrene-modified mesoporous organosilicas for acid-catalyzed processes, Chem. Eng. J. 161 (2010) 388-396.

[15] C.X. Lin, S.Z. Qiao, C.Z. Yu, S. Ismadji, G.Q. Lu, Periodic mesoporous silica and organosilica with controlled morphologies as carriers for drug release, Micropor. Mesopor. Mat. 117 (2009) 213-219.

[16] W. Guo, J. Wang, S.J. Lee, F. Dong, S.S. Park, C.S. Ha, A general pH-responsive supramolecular nanovalve based on mesoporous organosilica hollow nanospheres, Chem. Eur. J. 16 (2010) 8641-8646.

[17] N. Lu, Y. Tian, W. Tian, P. Huang, Y. Liu, Y. Tang, C. Wang, S. Wang, Y. Su, Y. Zhang, J. Pan, Z. Teng, G. Lu, Smart cancer cell targeting imaging and drug delivery system by systematically engineering periodic mesoporous organosilica nanoparticles, ACS Appl. Mater. Interfaces. 8 (2016) 2985-2993.

[18] Z. Teng, X. Su, Y. Zheng, J. Zhang, Y. Liu, S. Wang, J. Wu, G. Chen, J. Wang, D. Zhao, G. Lu, A facile multi-interface transformation approach to monodisperse multiple-shelled periodic mesoporous organosilica hollow spheres, J. Am. Chem. Soc. 137 (2015) 7935-7944.

[19] X. Yang, D. He, X. He, K. Wang, J. Tang, Z. Zou, X. He, J. Xiong, L. Li, J. Shangguan, Synthesis of hollow mesoporous silica nanorods with controllable aspect ratios for intracellular triggered drug release in cancer cells, ACS Appl. Mater. Interfaces. 8 (2016) 20558-20569.

[20] J. Wu, Y. Liu, Y. Tang, S. Wang, C. Wang, Y. Li, X. Su, J. Tian, Y. Tian, J. Pan, Y. Su, H. Zhu, Z. Teng, G. Lu, Synergistic chemo-photothermal therapy of breast cancer by mesenchymal stem cell-encapsulated yolk-shell GNR@HPMO-PTX nanospheres, ACS Appl. Mater. Interfaces. 8 (2016) 17927-17935.

[21] H.-J.G. N. S. Kehr, K. Riehemanna, H. Fuchsa, Self-assembled monolayers of enantiomerically functionalized periodic mesoporous organosilicas and the effect of surface chirality on cell adhesion behaviour, RSC Adv. 5 (2015) 5704–5710.

[22] J.H. Kim, B. Fang, M.Y. Song, J.-S. Yu, Topological transformation of thioether-bridged organosilicas into nanostructured functional materials, Chem. Mater. 24 (2012) 2256-2264.

[23] Z. Teng, S. Wang, X. Su, G. Chen, Y. Liu, Z. Luo, W. Luo, Y. Tang, H. Ju, D. Zhao, G. Lu, Facile synthesis of yolk-shell structured inorganic-organic hybrid spheres with ordered radial mesochannels, Adv. Mater. 26 (2014) 3741-3747.

[24] F. Muhammad, M. Guo, W. Qi, F. Sun, A. Wang, Y. Guo, G. Zhu, pH-Triggered controlled drug release from mesoporous silica nanoparticles via intracelluar dissolution of ZnO nanolids, J. Am. Chem. Soc. 133 (2011) 8778-8781.

[25] S. Niedermayer, V. Weiss, A. Herrmann, A. Schmidt, S. Datz, K. Muller, E. Wagner, T. Bein, C. Brauchle, Multifunctional polymer-capped mesoporous silica nanoparticles for pH-responsive targeted drug delivery, Nanoscale 7 (2015) 7953-7964.

[26] G. Chen, Y. Xie, R. Peltier, H. Lei, P. Wang, J. Chen, Y. Hu, F. Wang, X. Yao, H. Sun, Peptide-decorated gold nanoparticles as functional nano-capping agent of mesoporous silica container for targeting drug delivery, ACS Appl. Mater. Interfaces. 8 (2016) 11204-11209.

[27] X. Xu, S. Lü, C. Gao, C. Feng, C. Wu, X. Bai, N. Gao, Z. Wang, M. Liu, Self-fluorescent and stimuli-responsive mesoporous silica nanoparticles using a double-role curcumin gatekeeper for drug delivery, Chem. Eng. J. 300 (2016) 185-192.

[28] T.M. Guardado-Alvarez, L. Sudha Devi, M.M. Russell, B.J. Schwartz, J.I. Zink, Activation of snap-top capped mesoporous silica nanocontainers using two near-infrared photons, J. Am. Chem. Soc.135 (2013) 14000-14003.

[29] Y. Cai, P. Liang, Q. Tang, X. Yang, W. Si, W. Huang, Q. Zhang, X. Dong, Diketopyrrolopyrrole-triphenylamine organic nanoparticles as multifunctional reagents for photoacoustic imaging-guided photodynamic/photothermal synergistic tumor therapy, ACS Nano., 11 (2017) 1054-1063.

[30] X. Liu, X. Zhang, M. Zhu, G. Lin, J. Liu, Z. Zhou, X. Tian, Y. Pan, PEGylated Au@Pt nanodendrites as novel theranostic agents for computed tomography imaging and photothermal/radiation synergistic therapy, ACS Appl. Mater. Interfaces. 9 (2017) 279-285.

[31] L.M.ı.M. D. Jaque, B. del Rosal, P. Haro-Gonzalez, A. Benayas, J. L. Plaza, E.

Mart´ın Rodr´ıgueza. J. Garc´ı Sole, Nanoparticles for photothermal therapies, Nanoscale, 6 (2014) 9494-9530.

[32] J. Kim, J. Kim, C. Jeong, W.J. Kim, Synergistic nanomedicine by combined gene and photothermal therapy, Adv. Drug. Deliver. Rev. 98 (2016) 99-112.

[33] E. Roy, S. Patra, R. Madhuri, P.K. Sharma, Carbon dot/TAT peptide co-conjugated bubble nanoliposome for multicolor cell imaging, nuclear-targeted delivery, and chemo/photothermal synergistic therapy, Chem. Eng. J. 312 (2017) 144-157.

[34] S. Wang, K. Li, Y. Chen, H. Chen, M. Ma, J. Feng, Q. Zhao, J. Shi, Biocompatible PEGylated MoS_2 nanosheets: controllable bottom-up synthesis and highly efficient photothermal regression of tumor, Biomaterials 39 (2015) 206-217.

[35] S.S. Chou, M. De, J. Kim, S. Byun, C. Dykstra, J. Yu, J. Huang, V.P. Dravid, Ligand conjugation of chemically exfoliated MoS_2, J. Am. Chem. Soc. 135 (2013) 4584-4587.

[36] W.Z. Teo, E.L. Chng, Z. Sofer, M. Pumera, Cytotoxicity of exfoliated transition-metal dichalcogenides (MoS_2 , WS_2 , and WSe_2) is lower than that of graphene and its analogues, Chem. Eur. J. 20 (2014) 9627-9632.

[37] H. Zhang, G. Grüner, Y. Zhao, Recent advancements of graphene in biomedicine, J. Mater. Chem. B. 1 (2013) 2542.

[38] T. Liu, C. Wang, X. Gu, H. Gong, L. Cheng, X. Shi, L. Feng, B. Sun, Z. Liu, Drug delivery with PEGylated MoS_2 nano-sheets for combined photothermal and chemotherapy of cancer, Adv. Mater. 26 (2014) 3433-3440.

[39] Y. Li, H. Wang, L. Xie, Y. Liang, G. Hong, H. Dai, MoS_2 nanoparticles grown on graphene: an advanced catalyst for the hydrogen evolution reaction, J. Am. Chem. Soc.133 (2011) 7296-7299.

[40] W. Feng, L. Chen, M. Qin, X. Zhou, Q. Zhang, Y. Miao, K. Qiu, Y. Zhang, C. He, Flower-like PEGylated MoS_2 nanoflakes for near-infrared photothermal cancer therapy, Sci. Rep. 5 (2015) 17422.

[41] Y.T. Liu, Z.Q. Duan, X.M. Xie, X.Y. Ye, A universal strategy for the hierarchical assembly of functional 0/2D nanohybrids, Chem. Commun. 49 (2013) 1642-1644.

[42] W. Zhao, A. Li, C. Chen, F. Quan, L. Sun, A. Zhang, Y. Zheng, J. Liu, Transferrin-decorated, MoS_2-capped hollow mesoporous silica nanospheres as a self-guided chemo–photothermal nanoplatform for controlled drug release and thermotherapy, J. Mater. Chem. B 5 (2017) 7403-7414.

[43] J. Kim, H. Kim, W.J. Kim, Single-layered MoS_2-PEI-PEG nanocomposite-mediated gene delivery controlled by photo and redox stimuli, Small 12 (2016) 1184-1192.

[44] M.A.-M. Antonio Topete, Pablo Iglesias, Eva M. Villar-Alvarez, Silvia Barbosa,Jose´ A. Costoya, Pablo Taboada, V1´ctor Mosquera, Fluorescent drug-loaded, polymeric-based, branched gold nanoshells for localized multimodal therapy and imaging of tumoral cells, ACS nano 8 (2014) 2725–2738.

[45] N. Lu, P. Huang, W. Fan, Z. Wang, Y. Liu, S. Wang, G. Zhang, J. Hu, W. Liu, G. Niu, R.D. Leapman, G. Lu, X. Chen, Tri-stimuli-responsive biodegradable theranostics for mild hyperthermia enhanced chemotherapy, Biomaterials 126 (2017) 39-48.

[46] H. Lin, J. Wang, Q. Luo, H. Peng, C. Luo, R. Qi, R. Huang, J. Travas-Sejdic, C.-G. Duan, Rapid and highly efficient chemical exfoliation of layered MoS_2 and WS_2, J. Alloy. Compd. 699 (2017) 222-229.

[47] Y. Tang, H. Hu, M.G. Zhang, J. Song, L. Nie, S. Wang, G. Niu, P. Huang, G. Lu, X. Chen, An aptamer-targeting photoresponsive drug delivery system using "off-on" graphene oxide wrapped mesoporous silica nanoparticles, Nanoscale 7 (2015) 6304-6310.

- BSA-FA-modified MoS_2 capped periodic mesoporous organosilica was fabricated.
- The MoS_2 can prevent the loaded drugs from leaking during the blood circulation.
- The nanoplatforms showed excellent synergistic effect for cancer therapy.
- The therapeutic effects were evaluated systematically both in vitro and in vivo.

Graphical abstract

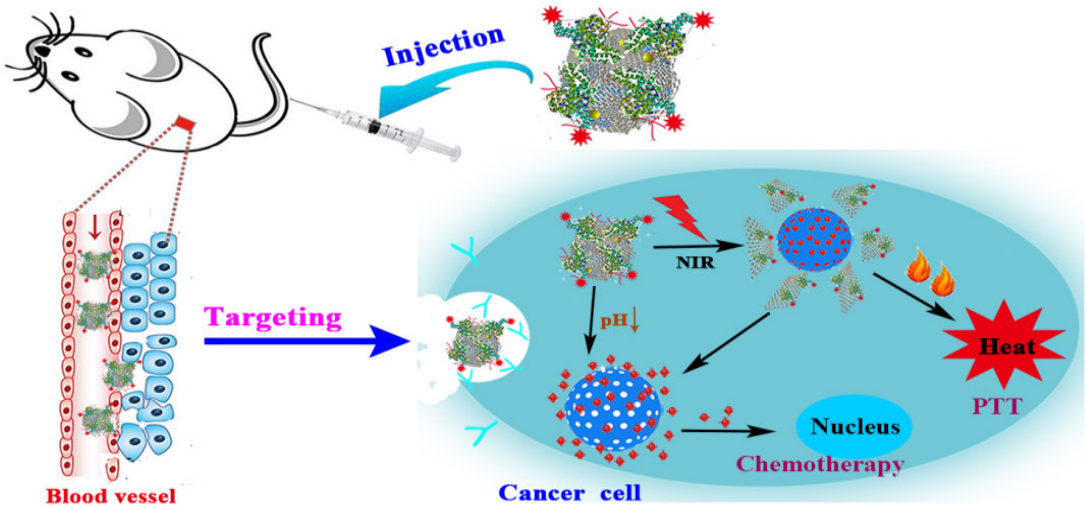

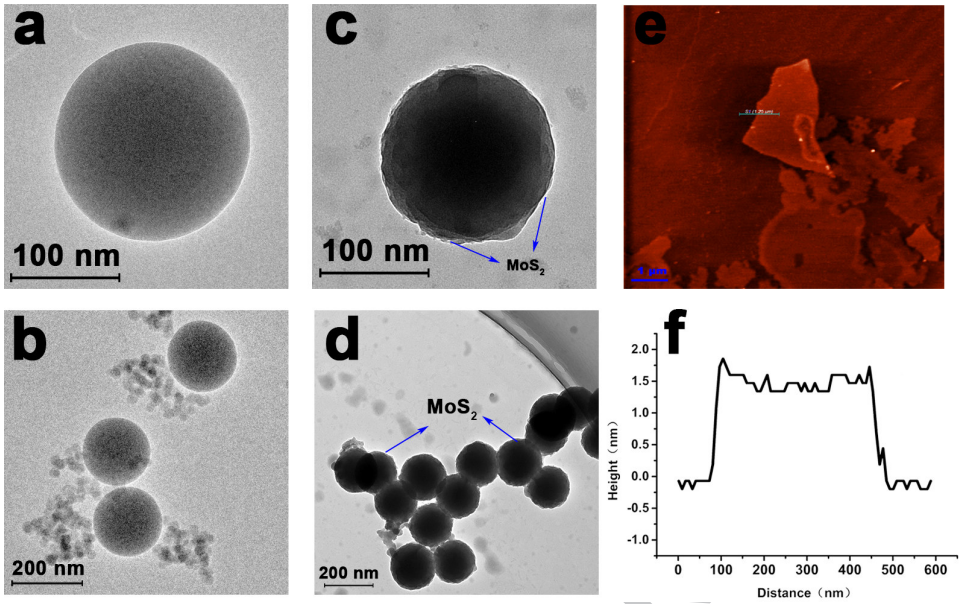

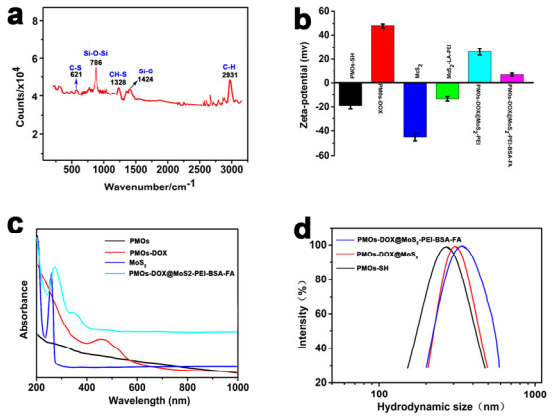

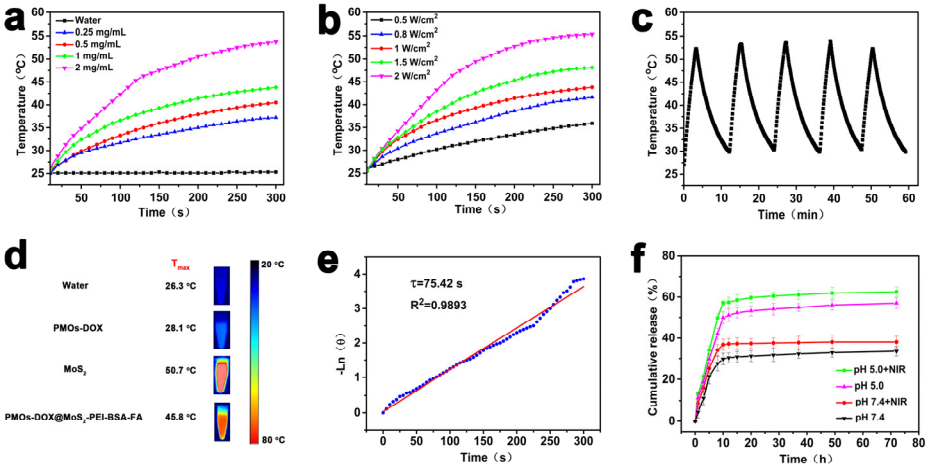

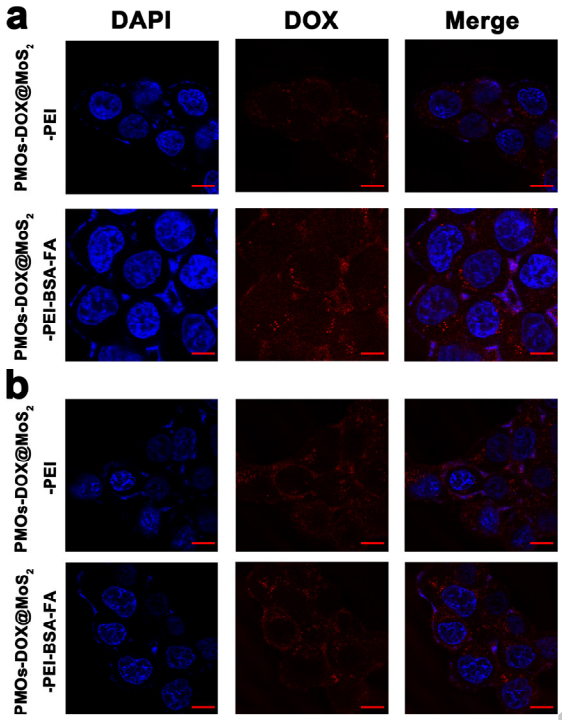

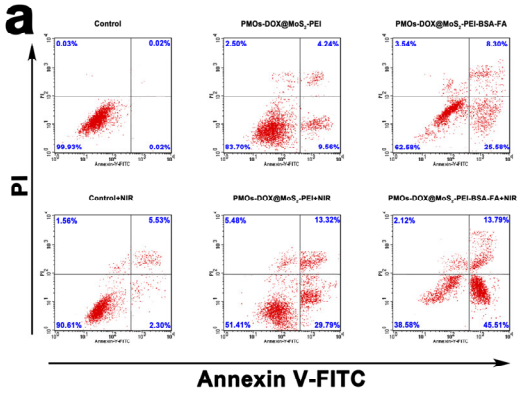

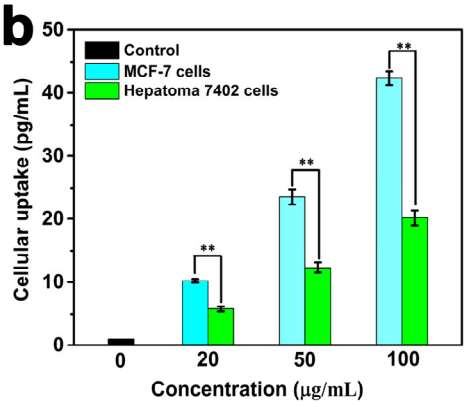

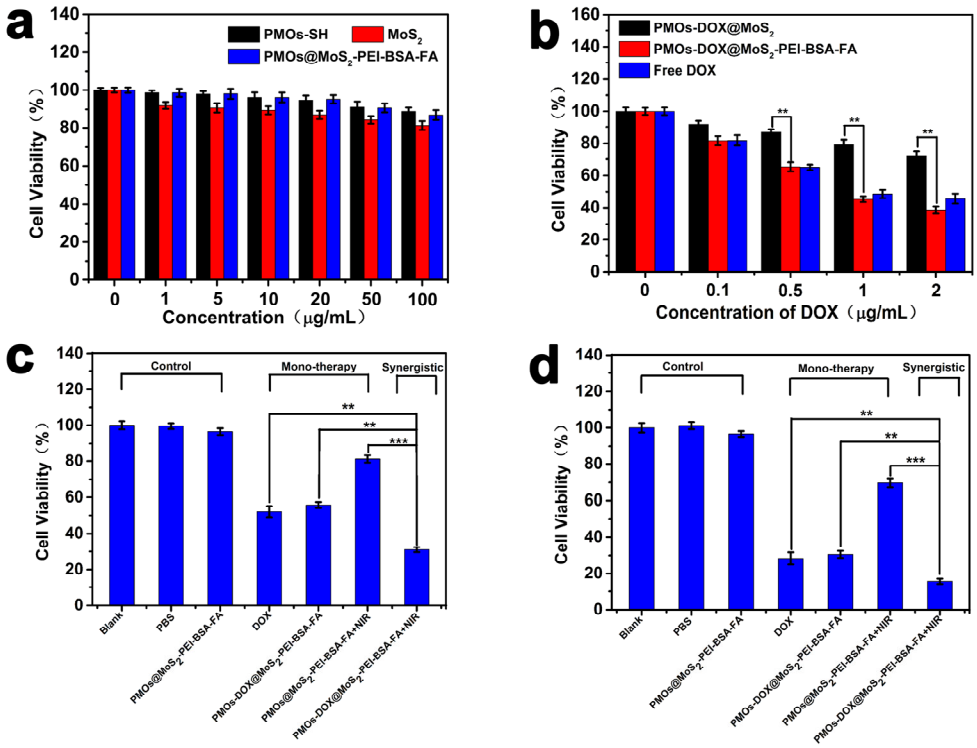

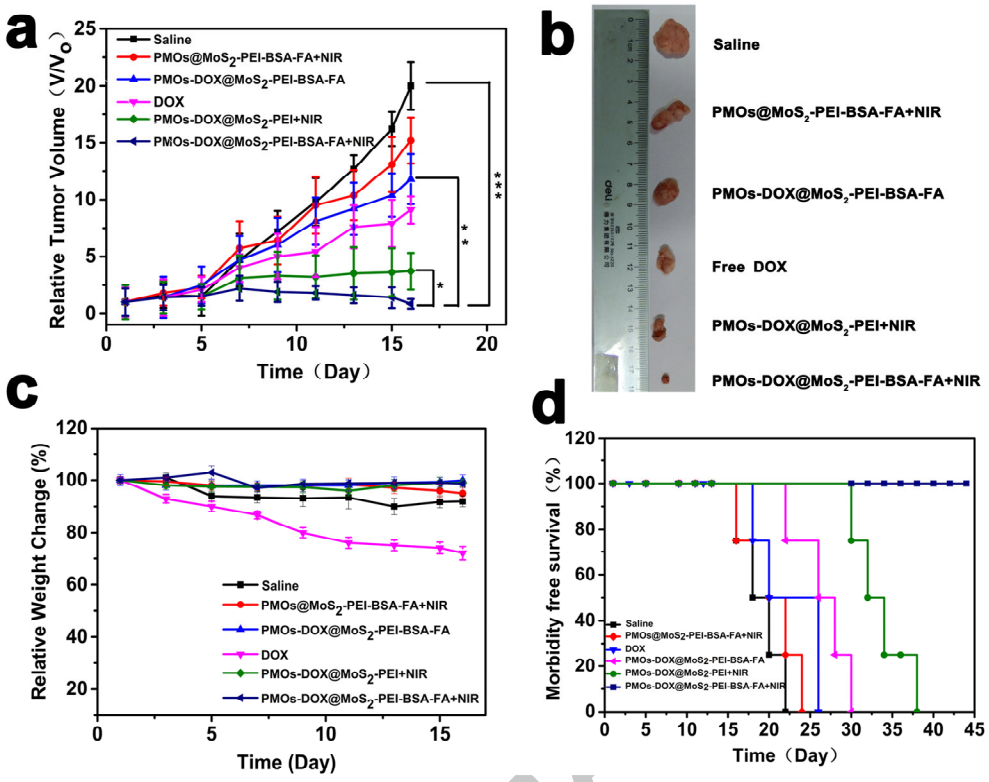
a
Relative Tumor Volume (V/V0)
Time (Day)
Saline
PMOs@MoS2-PEI-BSA-FA+NIR
PMOs-DOX@MoS2-PEI-BSA-FA
DOX
PMOs-DOX@MoS2-PEI+NIR
PMOs-DOX@MoS2-PEI-BSA-FA+NIR
b
Saline
PMOs@MoS2-PEI-BSA-FA+NIR
PMOs-DOX@MoS2-PEI-BSA-FA
Free DOX
PMOs-DOX@MoS2-PEI+NIR
PMOs-DOX@MoS2-PEI-BSA-FA+NIR
c
Relative Weight Change (%)
Time (Day)
d
Morbidity free survival (%)
Time (Day)

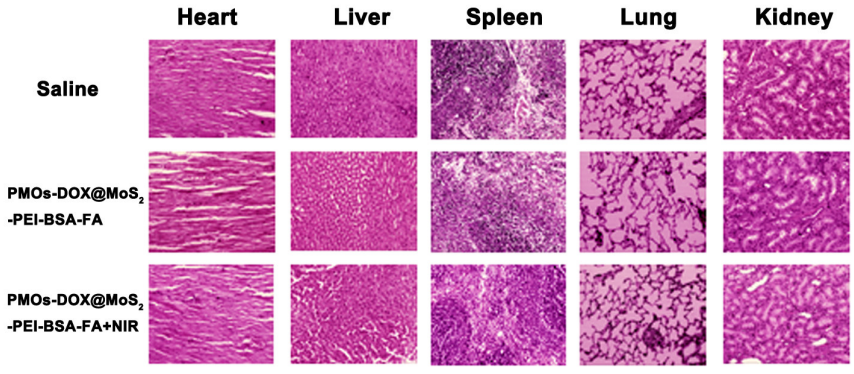
Heart
Liver
Spleen
Lung
Kidney
Saline
PMOs-DOX@MoS2 -PEI-BSA-FA
PMOs-DOX@MoS2 -PEI-BSA-FA+NIR